Time-of-Arrival of Coronal Mass Ejections: A Two-Phase Kinematics Approach Based on Heliospheric Imaging Observations

Evangelos Paouris[1] and Angelos Vourlidas[2]

[1]George Mason University
[2]JHU APL

November 22, 2022

Abstract

Despite the ability to image coronal mass ejections (CMEs) from the Sun through the inner heliosphere, the forecasting of their Time-of-Arrival (ToA) to Earth does not yet meet most Space weather users' requirements. The main physical reason is our incomplete understanding of CME propagation in the inner heliosphere. Therefore, many ToA forecasting algorithms rely on simple empirical relations to represent the interplanetary propagation phase using, mostly, kinematic information from coronagraphic observations below 30 solar radii (Rs) and a couple rather implying assumptions of constant direction and speed for the transient. Here, we explore a different, yet still empirical approach. We replace the assumption of constant speed in the inner heliosphere with a two-phase behavior consisting of a decelerating (or accelerating) phase from 20 Rs to some distance, followed by a coasting phase to Earth. In a nod towards a forecasting scheme, we consider only Earth-directed CMEs use kinematic measurements only from the Heliospheric Imagers aboard both STEREO spacecraft, treat each spacecraft separately to increase the event statistics, analyze the measurements in a data-assimilative fashion and intercompare them against three popular localization schemes for single viewpoint observations (fixed-φ, harmonic mean and self-similar expansion. For the 21 cases, we obtain the best mean absolute error (MAE) of 6.4±1.9 hours, for the harmonic mean approximation. Remarkably, the difference between predicted and observed ToA is < 52 minutes for 42% of the cases. We find that CMEs continue to decelerate beyond even 0.7 AU, in some cases.

Hosted file

`essoar.10510653.1.docx` available at https://authorea.com/users/535320/articles/598724-time-of-arrival-of-coronal-mass-ejections-a-two-phase-kinematics-approach-based-on-heliospheric-imaging-observations

1 **Time-of-Arrival of Coronal Mass Ejections: A Two-Phase Kinematics Approach Based on**
2 **Heliospheric Imaging Observations**
3

4 **Evangelos Paouris[1,2] and Angelos Vourlidas[2]**

5 [1]George Mason University, Fairfax, VA, USA.

6 [2]The Johns Hopkins University Applied Physics Laboratory, Laurel, MD, USA.

7

8 Corresponding author: Evangelos Paouris (evpaouris@noa.gr)

9 **Key Points:**

10 • We approach the inner heliospheric propagation of coronal mass ejections as a two-phase
11 behavior of deceleration followed by coasting

12 • The lowest mean absolute ToA error is 6.4 hours for a sample of 19 events for harmonic
13 mean technique

14 • Our data-assimilative approach indicates reasonable forecasts with a mean lead time of
15 31 hours
16

Abstract

Despite the ability to image coronal mass ejections (CMEs) from the Sun through the inner heliosphere, the forecasting of their Time-of-Arrival (ToA) to Earth does not yet meet most Space weather users' requirements. The main physical reason is our incomplete understanding of CME propagation in the inner heliosphere. Therefore, many ToA forecasting algorithms rely on simple empirical relations to represent the interplanetary propagation phase using, mostly, kinematic information from coronagraphic observations below 30 solar radii (Rs) and a couple rather implying assumptions of constant direction and speed for the transient. Here, we explore a different, yet still empirical approach. We replace the assumption of constant speed in the inner heliosphere with a two-phase behavior consisting of a decelerating (or accelerating) phase from 20 Rs to some distance, followed by a coasting phase to Earth. In a nod towards a forecasting scheme, we consider only Earth-directed CMEs use kinematic measurements only from the Heliospheric Imagers aboard both STEREO spacecraft, treat each spacecraft separately to increase the event statistics, analyze the measurements in a data-assimilative fashion and intercompare them against three popular localization schemes for single viewpoint observations (fixed-φ, harmonic mean and self-similar expansion. For the 21 cases, we obtain the best mean absolute error (MAE) of 6.4±1.9 hours, for the harmonic mean approximation. Remarkably, the difference between predicted and observed ToA is < 52 minutes for 42% of the cases. We find that CMEs continue to decelerate beyond even 0.7 AU, in some cases.

Plain Language Summary

Solar eruptive phenomena like the coronal mass ejections (CMEs) are able nowadays to affect almost every aspect of human activity in space or on the ground and human life. The early and valid prediction of the impact of these events on Earth is one of the most important open research fields. We propose a new way to use data from heliospheric imagers (HIs) onboard STEREO spacecraft which observe the area between the Sun and the Earth. In all previous published works where utilized data from HIs the CME propagation assumed as a constant speed movement. In our work we track CMEs in the inner heliosphere and we apply a simple and at the same time realistic scenario for their propagation. We assume that all CMEs, after their eruption from the solar atmosphere, are accelerating (or decelerating) to some distance, followed by a coasting phase to Earth. We found the lowest mean absolute error (MAE)between the predicted and the observed arrival times of CMEs to Earth was 6.4 hours for a sample of 19 cases. This value is almost 3.5 hours lower than the MAE which occurs from the approach of constant speed movement.

1 Introduction

The Coronal Mass Ejections (CMEs) are solar eruptions of great interest as their interplanetary counterparts (ICMEs) trigger the most intense geomagnetic storms (see e.g. Tsurutani and Gonzalez, 1997; Richardson et al., 2006; Zhang et al., 2007; Paouris and Mavromichalaki, 2017a; Paouris et al., 2021a and references therein). CMEs are primarily observed by white light coronagraphs like the Large Angle and Spectroscopic Coronagraph (LASCO; Brueckner et al., 1995) aboard the Solar and Heliospheric Observatory (SOHO; Domingo et al., 1995) and the Sun Earth Connection Coronal and Heliospheric Investigation (SECCHI) instruments (Howard et al., 2008) aboard the Solar TErrestrial RElations Observatory (STEREO) mission (Kaiser et al., 2008). The STEREO mission inaugurated a new era in Heliophysics research by offering the unique opportunity to simultaneously observe the same CME, with identical instrumentation, from two

61   vantage points along the full Sun-Earth line. This capability drove a large amount of research and
62   technique development to estimate the properties of CMEs (angular width, linear speed, mass,
63   propagation direction, etc.) based on multi-view point observations (see e.g. Mierla et al., 2008;
64   Howard & Tappin, 2008; Temmer et al., 2009; Lee et al., 2015; Jang et al., 2016; Vourlidas et al.,
65   2017; Balmaceda et al., 2018).
66   The SECCHI payload includes a Heliospheric Imager (HI), consisting of two cameras (Eyles et
67   al., 2009). The inner camera (HI-1) field of view (FOV) extends from 4° to 24° and is centered at
68   14° elongation from Sun center. The outer camera (HI-2) FOV extends between 18.7°-88.7°
69   centered at 53.7° from Sun center. This instrument can observe a CME from a distance of 15 up
70   to 330 solar radii (Rs), approximately. Taking radial slices from combined HI-1 and HI-2 running-
71   difference images along a given position angle (PA) and then stacking them as a function of time
72   results in time-elongation maps, or so-called J-maps (see e.g. Sheeley et al., 1999; 2008; Barnes et
73   al., 2019 and references therein). Any outward propagating structure is easily spotted in J-maps as
74   a bright ridge. The tracking of a feature, e.g. the CME front, in J-maps provides the elongation
75   angles as a function of time. the most important questions for space weather forecasting are: *when
76   will the CME arrive* and *how strong the impact will be*. The answers to these are provided by three
77   quantities: the Time-of-Arrival (ToA), the Speed-on-Arrival (SoA) and the magnitude of the
78   southward component of the ICME magnetic field (see e.g. Vourlidas, 2019; Paouris et al.,
79   (2021b), hereafter referred to as P21). Here we focus mainly on the ToA and partially on the SoA
80   issues.
81   Several methods have been developed to derive the propagation direction and speed of the transient
82   under various geometric and kinematic assumptions. The two most common assumptions are that
83   the CME propagates (1) at a constant speed and (2) along a fixed radial direction in the FOV of
84   the HI.
85   *But how accurate are these assumptions?* This is actually the question we want to answer here.
86   Regarding the fixed radial direction, several published works suggest that CME does indeed
87   propagate away from the Sun in a constant propagation direction. On the other hand, several
88   phenomena which may affect the propagation direction have been identified, such as latitudinal
89   and longitudinal deflections (Byrne et al., 2010; Isavnin et al., 2013; Kay et al., 2013; 2015), non-
90   uniform expansion in the lower corona (e.g. Nieves-Chinchilla et al., 2012) and CME/CME
91   interactions (Lugaz et al., 2012). These analyses report that these phenomena take place close to
92   the Sun (d < 10 Rs). It appears, therefore, that the CME propagation along a fixed radial direction,
93   especially for distances d > 50 Rs (approximately the HI-1 FOV center), should be a reasonable
94   assumption.
95   On the other hand, the assumption of CME propagation at constant speed within the HI FOV is
96   rather weak. It is generally assumed that CMEs reach their final speed at radial distances below
97   20-40 Rs (Vrsnak et al., 2004; Vrsnak et al., 2013). However, other works suggest that the
98   acceleration of slow CMEs and the deceleration of fast CMEs continues for greater distances, even
99   as far as the Venus orbit (0.72 AU ≈ 155 Rs). In particular, Gopalswamy et al. (2001) found an
100   acceleration cessation distance of 0.76 AU. Manoharan et al., (2001) studied an Earth-directed fast
101   halo CME occurred on July 14, 2000 associated with a X5.7 solar flare. Using data from many
102   instruments created the speed profile of the CME as a function of the heliocentric distance. They
103   found a two-level deceleration: 1) a slow decrease of the CME speed from launch to 100 Rs and
104   2) a rapid decrease at larger distances (r > 100 Rs) from the Sun. Reiner et al., (2007) studied a
105   sample of 42 fast and very fast ICMEs (mean $V_{LASCO} \approx 1600$ km/s) and their associated shocks
106   observed during solar cycle 23. In all cases they found a deceleration cessation distance greater

107   than 0.27 AU (r ≈ 58 Rs) with a mean value of 0.65 AU (r ≈ 140 Rs). Liu et al., (2013) studied
108   three ICMEs and found that the rapid deceleration occurs over a relatively short timescale
109   following the acceleration phase. The rapid deceleration lasts about 5 to 10 hours and the cessation
110   distance is between 40 and 80 Rs from Sun center. Winslow et al., (2015) used data from the
111   MErcury Surface, Space ENvironment, GEochemistry, and Ranging (MESSENGER) spacecraft,
112   to investigate ICMEs around orbit Mercury (0.31-0.47 AU). In a sample of 61 ICMEs, they found
113   that the speed decrease is possible to occur everywhere between Mercury's orbit and 1 AU. Wood
114   et al., (2017) studied a sample of 28 ICMEs and they found that the CMEs reached their final
115   speeds at distances ranging from 4.8 Rs up to 198.7 Rs while almost 40% of the events reached
116   the final speed at heights of 65 Rs. They noted that it is likely that many CMEs still exhibit some
117   degree of deceleration at 1 AU. Recently, Paouris et al., (2021a), examined the scenario of a more
118   effective deceleration in the interplanetary medium. This scenario was tested with the Effective
119   Acceleration Model (EAM) and the Drag Based Model (DBM). In particular, they estimated, for
120   a sample of 16 fast ICMEs, the distance where the initial CME speed becomes equal to the
121   corrected speed from the EAM model. It was possible to calculate these distances, for 11 cases,
122   resulting in a mean cessation distance of 0.72 AU (r ≈ 155 Rs. They presented, for the first time,
123   to the best of our knowledge, a comparison of the performance of three different CME propagation
124   models in estimating of the Time-of-Arrival (ToA) of CMEs to 1 AU; namely, an empirical data
125   driven model (EAM – Paouris and Mavromichalaki, 2017b), a drag-based ensemble model
126   (DBEM – Dumbovic et al., 2018) and an MHD analytical model (WSA-ENLIL+Cone model –
127   Mays et al., 2015) using the same CME/ICME sample and the same statistical metrics. The
128   performance of the DBEM model improved significantly when greater values for the drag
129   parameter were used. The optimal drag parameter was larger than the values used in Dumbovic et
130   al., 2018 (i.e. 0.1 x 10^{-7} km^{-1}) by a factor of 2.1-4.8. Calogovic et al., 2021, also showed that the
131   optimal drag parameter value is in higher by a factor of 3 compared to Dumbovic et al., 2018. This
132   underestimate of the drag parameter indicates a stronger deceleration of the ICMEs in the
133   interplanetary medium (see Paouris et al., (2021a) for details).
134   All previous approaches (Sheeley et al., 1999; 2008; Kahler and Webb, 2007; Rouillard et al.,
135   2008; Lugaz et al., 2009; Lugaz et al., 2010; Davies et al., 2012; Barnes et al., 2019; Möstl et al.,
136   2011; Möstl and Davies, 2013; Möstl et al., 2014) assumed constant propagation and speed to fit
137   the measured elongation angles as a function of time. The best-fit values of direction and speed
138   were then obtained by the minimum standard deviation of the residuals (see Lugaz 2010). Möstl
139   et al., 2014 mentioned that the inclusion of a more realistic approach which will take into account
140   the deceleration into the geometrical single-spacecraft fitting methods will further improve the
141   accuracy of predicting CME arrival times and speeds instead of the current assumption of constant
142   speed. This is the motivation behind this paper.

143   We take the following approach. We transform the observed elongation angles versus
144   time, a(t), into radial distances versus time r(t) via techniques such as: a) the Fixed –Phi (FP)
145   approximation (Sheeley et al., 1999; 2008; Kahler and Webb, 2007; Rouillard et al., 2008), b)
146   the Harmonic Mean (HM) approximation (Lugaz et al., 2009), and c) the Self-Similar Expansion
147   (SSE) approximation (Lugaz et al., 2010; Davies et al., 2012; Möstl and Davies, 2013). We then
148   assume that all CMEs could accelerate or decelerate up to a distance from Sun and then they
149   coast at a constant speed. Applying simple kinematic equations, we estimate the ToA at 1 AU
150   utilizing the previous techniques. We call this the two-phase kinematics and present our
151   methodology in the next section (Section 2). The impact of this approach on the ToA as well as

152 the Speed-on-Arrival (SoA) of the ICME at 1 AU are presented in Section 3. In Section 4, we
153 present our conclusions and a discussion on the results.

154

2 Data Sources and Methodology

156   2.1 Events for analysis

157 We want to test the effect of the assumptions of constant speed and constant propagation angle on
158 ToA estimates, using the HI observations. We are going to assume that CMEs accelerate (or
159 decelerate) from the Sun up to a certain distance in the inner heliosphere. Beyond that distance,
160 the CMEs propagate at constant speed until they reach Earth. Similar approaches for CME
161 kinematics have been presented before (see e.g., Reiner et al., 2007; Wood et al., 2017). We refer
162 to this profile as "two-phase" kinematics. We apply this approach to a sample of 13 CMEs/ICMEs
163 observed by a combination of SOHO, STEREO-A (ST-A), and STEREO-B (ST-B). Here, we
164 apply our technique using data from only the STEREO/HIs. The SOHO coronagraph data provide
165 constraints on the CME direction and ensure that we are dealing with Earth-directed events.
166 Each CME in the HIGeoCAT catalog (Barnes et al., 2019 ; https://www.helcats-
167 fp7.eu/catalogues/wp3_cat.html) was analyzed with the geometrical-fitting techniques of FP, HM
168 and SSE, independently for each STEREO/HI. Thus, we can also treat those observations as
169 'separate events' to increase our sample to 21 cases. The selected CMEs are presented in Table 1.
170 The first three columns show the LASCO CME onset date, time and linear speed, the fourth
171 column marks the ST-A/-B availability of HI data, and the last two columns show the magnitude
172 and the heliographic latitude and longitude of the associated solar flare.

173

Table 1. CME onset time and the associated solar flares used in our study.

CME onset (LASCO)			STEREO A/B	Solar Flare	
Date	*Time*	*Linear speed (km/s)*	*HI availability[a]*	*Magnitude*	*Heliographic coordinates*
03/04/2010	10:34	668	A/B	B7.4	S25W03
15/02/2011	02:24	669	A/B	X2.2	S20W10
07/03/2011	14:48	698	Only ST-B	M2.0	N11E21
07/03/2011	20:00	2125	Only ST-A	M3.7	N30W48
04/08/2011	04:12	1315	A/B	M9.3	N15W39
11/04/2013	07:24	861	A/B	M6.5	N07E13
21/06/2013	03:12	1900	Only ST-A	M2.9	S14E37
29/09/2013	20:40	1179	A/B	_[b]	N20W30
07/01/2014	18:24	1830	Only ST-A	X1.2	S15W10
25/02/2014	01:09	2147	A/B	X4.9	S15E77
02/04/2014	13:36	1471	A/B	M6.5	N12E53
18/04/2014	13:09	1203	A/B	M7.3	S18W29
07/12/2020	16:24	1407	Only ST-A	C7.4	S23W11

*a: If data from both HI cameras are available then we set the indicator "*A/B*". For unique data availability we note which of STEREO-A or -B was available.*

b: This CME is associated with an active region with known coordinates.

174

175   2.2 Geometric Techniques

176 The availability of heliospheric imaging from the two vantage points of STEREO satellites led to
177 the development of many techniques based on the time-elongation profiles to estimate the speed
178 and the direction of the CME in 3D space. The Fixed-Phi (FP) approximation (Sheeley et al., 1999;
179 2008; Kahler and Webb, 2007; Rouillard et al., 2008) treats the CME as a relatively compact
180 structure (point source) moving along a fixed radial direction.
181 The radial distance using the FP is given by the equation:

182
$$r_{FP} = \frac{d_{SC} \cdot \sin\alpha}{\sin(\alpha + \varphi)} \quad (1)$$

183 Where d_{SC} is the spacecraft-sun distance, a, is the elongation of the CME front, and φ is the
184 Observer-Sun-CME angle.
185 The Harmonic Mean (HM) method (Lugaz et al., 2009) assumes that the CME is represented by a
186 circle anchored at the Sun expanding along a fixed radial direction, which results in

187
$$r_{HM} = \frac{2d_{SC} \cdot \sin\alpha}{1 + \sin(\alpha + \varphi)} \quad (2)$$

188 Finally, the Self-Similar Expansion (SSE) approximation (Lugaz et al., 2010; Davies et al., 2012)
189 assumes the CME as an expanding circle which propagates radially but with a fixed half-width (λ).
190 The radial distances are calculated by the equation:

191
$$r_{SSE} = \frac{d_{SC} \cdot \sin\alpha \cdot (1 + \sin\lambda)}{\sin\lambda + \sin(\alpha + \varphi)} \quad (3)$$

192 The equation reduces to the FP and the HM equations for the cases of $\lambda = 0°$ and $\lambda = 90°$.
193 The three approximations (FP, HM and SSE) have been used extensively (Sheeley et al., 1999;
194 2008; Kahler and Webb, 2007; Rouillard et al., 2008; Lugaz et al., 2009; Lugaz et al., 2010;
195 Davies et al., 2012; Barnes et al., 2019; Möstl et al., 2011; Möstl and Davies, 2013; Möstl et al.,
196 2014) under the two basic assumptions of constant propagation direction and constant speed.
197 Equations (1), (2) and (3) estimate the CME radial distance as a function of the measured
198 elongation angle. First, under the assumption of constant speed, the radial distance r is replaced
199 by the product Vt, where V is the constant speed and t is the time. Then, the distances are
200 inverted to elongation angles (Appendix I). We refer to these as the "theoretical profiles". The
201 measured elongation-time profiles from the HI data, are then fitted to these theoretical profiles.
202 Since there exist many possible solutions of pairs (φ, V), the pair that minimizes the standard
203 deviation of the residual is selected as the best fit (Barnes et al., 2019). A comprehensive
204 analysis on the accuracy as well as the limitations of these methods is presented in Lugaz (2010).
205

206   2.3 Proposed Methodology

207 Equations (1)-(3) indicate that the necessary parameters for the transformation from elongation
208 to radial distance are: the heliocentric distance of the observer (d_{SC}), the observed elongation
209 angle (a), the Observer-Sun-CME or exit angle (φ) and the half-angular width of the CME (λ).
210 We obtain these parameters for each CME as follows:
211   •   We use $\lambda = 33.75°$ for all cases. As we argued in P21 and in Vourlidas et al. (2017), the
212   widths of CME can be bounded by the typical widths of flux-rope (F-Type) and the loop
213   (L-Type) CMEs, as these two types represent the two projections of a typical flux-rope
214   CME. Under the assumption that L-Type (F-Type) CMEs are CMEs face-on (edge-on),

215   we use 94° as the upper limit and 41° as the lower limit for the angular width (see [P21](#) for
216   details). In the SSE approximation we use the average of the two upper and lower limits
217   (33.75°) as the half-width.

218 • The distance between the observer and the Sun (d_{SC}) is available through the SPICE
219   routines in IDL for a given date and time.

220 • The elongation-time measurements are taken from the HIGeoCAT catalog
221   (https://www.helcats-fp7.eu/catalogues/wp3_cat.html). A detailed description of
222   HIGeoCAT is given by [Barnes et al., 2019](#). The arrival times for HIGeoCAT CMEs were
223   obtained from the ARRival CATalog (ARRCAT; [https://www.helcats-](https://www.helcats-fp7.eu/catalogues/wp4_arrcat.html)
224   [fp7.eu/catalogues/wp4_arrcat.html](https://www.helcats-fp7.eu/catalogues/wp4_arrcat.html)). ARRCAT lists predicted arrival time and speeds of
225   CMEs at various spacecraft and planets with the STEREO heliospheric imager
226   instruments, between April 2007 - September 2014. These arrival times calculated with
227   the SSE approximation (with $\lambda = 30°$) from [Möstl and Davies (2013)](#). We also use the
228   Space Weather Database of Notifications, Knowledge, Information (DONKI) to search
229   for associations between the CMEs and solar flare activity.

230 • Finally, we adopt two methods to estimate the Observer-Sun-CME angle, φ: (1) we use
231   the φ angle from the HIGeoCAT catalogue for each one of the three approximations; (2)
232   we assume the CME is propagating radially above the flare location (see [P21](#)); hereafter
233   referred to as the flare-site assumption. In this case, the φ angle is the heliographic
234   location (φ_{flare}) of the flare relative to the the spacecraft). Hence, we test our ToA
235   predictions with four different φ. We choose to include the estimation of φ from the flare
236   location because of its potential utility in a CME propagation forecasting tool. On the
237   contrary, the HIGeoCAT φ parameter is derived after all the HI data become available
238   and the fitting is performed. This process is not compatible with a real-time application.

239 • *Critical angles and projection effects*. The trigonometrical nature of equations (1)-(3)
240   may lead to unphysical distances for certain critical angles. We count those cases as fails
241   (F). For example, as the sum $a+\varphi$ approaches 180° in the FP approximation, eq (1)
242   approaches infinity. In the HM approximation, infinity occurs when the sum $a+\varphi$ in the
243   denominator of equation (2) approaches 270°. This situation can occur under the flare-
244   site assumption for 60° elongation angle and direction φ of 210° (φ is the sum SC_{angle} +
245     $|\varphi_{flare}|$, as described before). For the SSE approximation, this situation arises when $\sin\lambda =$
246   - $\sin(a+\varphi)$ or the sum $a+\varphi = 180° + \lambda = 213.75°$, where λ in our work is always equal to
247   33.75°. We came across these unphysical results with angles φ from both the HIGeoCAT
248   catalogue and the flare-site assumption. Hence, angles close to the critical angles could
249   potentially lead to unphysical results (i.e., unreasonably high accelerations or SoAs) and
250   thus each prediction should be examined carefully. Another important caveat is the effect
251   of projection on the transformation of elongation angle to radial distance. [Sheeley et al.,](#)
252   [1999](#), report that when a transient is propagating away from the sky plane there is an
253   additional contribution to the apparent acceleration, even if the transient propagates at
254   constant speed.

255 • Once we have these values, we are ready to fit the kinematic profile.

256

257
$$r(t) = c_1 t_{d_1-d_2}^2 + c_2 t_{d_1-d_2} + c_3 \quad (4)$$

258

259   Equation 4 represents the 2nd order polynomial fit we apply to the distances (r) vs. time
260   (t) for the first phase of the accelerating (or the decelerating) movement of the ICME

261 which is bounded to the radial distances d_1 and d_2. Then, from the distance d_2 up to 1 AU
262 we assume constant speed. The factors c_i ($i = 1$ to 3) are calculated by the polynomial fit.
263 In particular, the acceleration (or deceleration) of the ICME is equal to 2.0 x c_1 and the c_2
264 represents the theoretical initial speed of the ICME at time $t_0 = 0$. Finally, c_3 is the radial
265 distance at time $t_0 = 0$.

266 • To simulate a real-time forecasting process, we treat the HI observations as real-time
267 data. The forecasting algorithm (HeRPA – *Heliospheric Reconstruction and Propagation*
268 *Algorithm*) begins when at least three elongation-time measurements become available.
269 We use equations (1)-(3) to obtain the radial distance profile for each of the three
270 geometrical assumptions. Then, we apply equations (4) to obtain the acceleration (or
271 deceleration) of the CME. This estimate is referred to time *t*. We repeat the procedure as
272 additional distance-time measurements become available. This updated acceleration is
273 referred to time *t*+1. The process continues for all the available points *N* (*N* is the total
274 number of radial distances vs. time). The result is the acceleration profile. Positive values
275 indicate acceleration while negative values indicate deceleration. We demonstrate the
276 procedure with an example in the next section.

277

3 Case Study of August 4, 2011 CME

279 The event on August 4, 2011 is an appropriate example as the HeRPA algorithm resulted in neither
280 the best nor the worst results. The CME was observed by SOHO, ST-A and ST-B. It appeared in
281 the FOV of LASCO/C2 coronagraph on August 4, 2011 at 04:12 UT and was accompanied by a
282 GOES M9.3 solar flare, peaking at 03:57 UT, from AR11261 (N15W39). This was an Earth-
283 directed CME with a linear speed of 1315 km/s, according to LASCO CME catalogue. The CME
284 arrived at Earth on August 5, 2011 at 17:20 UT and triggered a severe geomagnetic storm with
285 maximum Ap index of 179 nT on August 5 (21:00 – 23:59 UT) and minimum Dst index of -115
286 nT on August 6 (03:00 – 03:59 UT). The average transit speed of the CME was 1135 km/s. This
287 rather high transit speed is likely due to a previous event that affected the background conditions
288 in the interplanetary medium clearing the path for this CME. The preconditioning of interplanetary
289 space described in Temmer et al., (2017).
290 ST-A and -B were separated by 167°, at the time of the CME launch. The estimated CME
291 directions from the HIGeoCAT database are plotted in the top panels of Figure 1. The propagation
292 direction (angle φ) for each geometrical method and the radial direction from the associated solar
293 flare are represented with colored arrows: blue for FP, black for HM, red for SSE and orange for
294 flare-based direction. The direction φ for radial propagation from the flare site is obtained by the
295 sum of the Spacecraft-Earth separation angle ($SC_{angle} = 100°$ for ST-A, $SC_{angle} = 93°$ for ST-B) and
296 the flare longitude (+39°) as follows: $\varphi_{FL|A} = SC_{angle|A} - |\varphi_{flare}| = 100° - |+39°| = 61°$, and $\varphi_{FL|B} =$
297 $SC_{angle|B} + |\varphi_{flare}| = 93° + |+39°| = 132°$ for ST-A and -B respectively.
298 The bottom panels of Figure 1 show the radial distances as a function of time for each geometrical
299 method using the time-elongation profiles from ST-A (left) and ST-B (right) with the same color
300 code for FP, HM and SSE as in the top panels.
301 We see that the CME direction as estimated by the geometric approximations is inconsistent
302 between ST-A and -B, indicating that projection effects may be affecting the measurements. This
303 is especially true for the HM approximation. The HM-based direction using φ from HIGeoCAT
304 lies close to the Sun-spacecraft line leading to unphysical SoA speeds and early predictions (black
305 points in middle row, Figure 1). This is expected. The φ_{HM} for both cases (ST-A and -B) has a

306   large angle of 159° and 170° respectively, indicating that the CME is moving away from the
307   spacecraft, and that creates an additional apparent acceleration, as discussed in subsection 2.3.
308   The bottom row of Figure 1 contains the radial distances as a function of time estimated under the
309   flare-site assumption. It is remarkable that all the geometrical approaches (FP, HM and SSE) are
310   providing identical results for ST-A (bottom left panel). The explanation lies in the value of $\varphi_{FL|A}$
311   = 61.3°. For this angle all trigonometrical functions in equations (1) - (3) have nearly the same
312   ratio for a given elongation angle. For ST-B (bottom right panel) we see that the slope of the points
313   from FP approximation leads to nonphysical SoA and an early prediction as a result of the angle
314    $\varphi_{FL|B} + a$. This angle is the sum of $\varphi_{FL|B} = 131.9°$ and the elongation angles a varying from 5.7° up
315   to 33.6°. As mentioned before in section 2.3 as the sum $a+\varphi$ approaches 180° in the FP
316   approximation, Eq (1) approaches infinity.

317
318
319
320
321
322
323
324
325
326
327
328
329
330
331
332
333
334
335
336
337
338
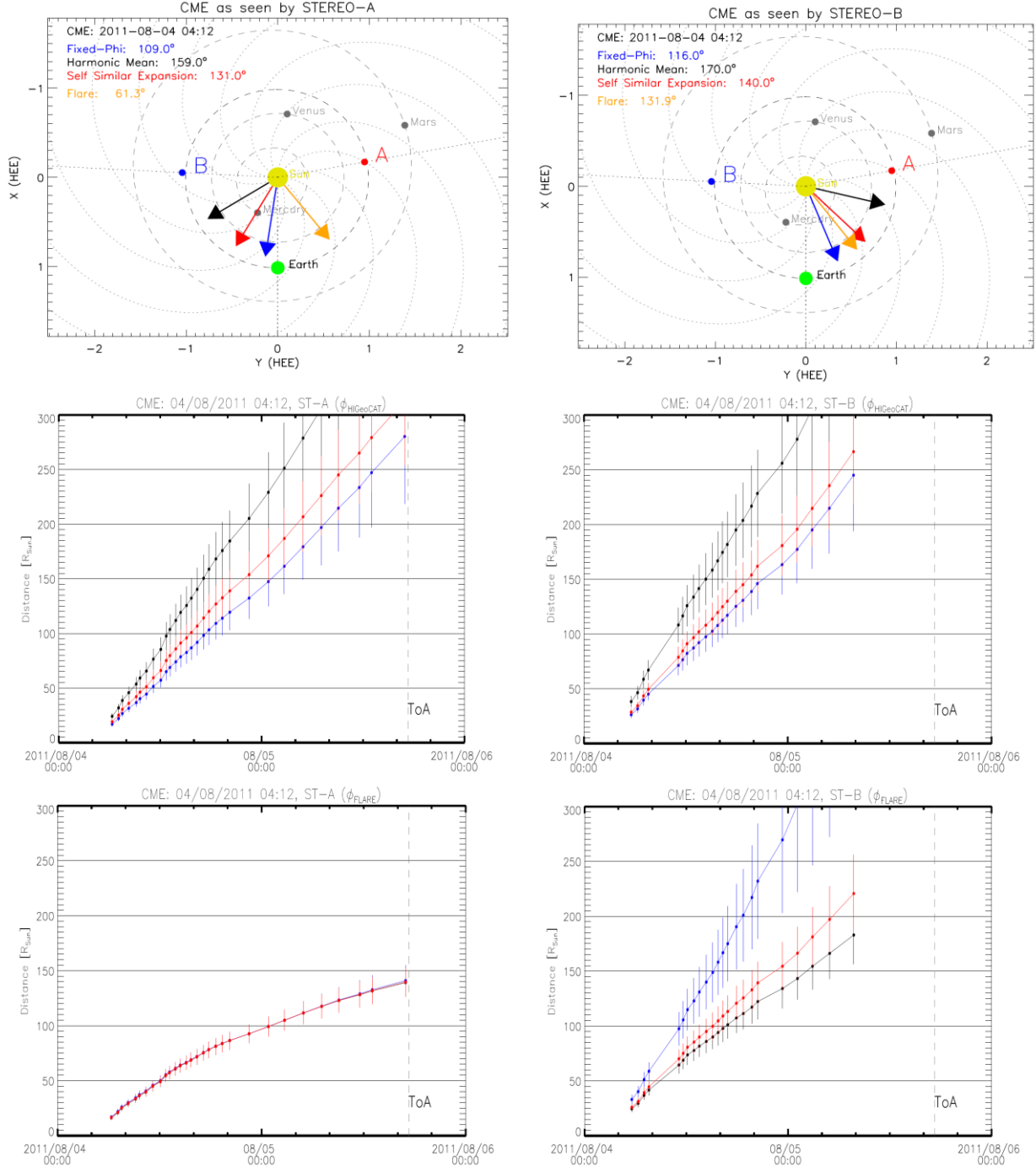339
340
341
342
343
344
345

Figure 1. *Propagation directions (φ) for August 04, 2011 CME for FP (blue), HM (black) and SSE (red) approximations for STEREO-A (top row - left) and -B (top row - right). The radial direction of the associated M9.3 solar flare is also indicated (orange arrow). The radial distances, and their errors, as a function of time for FP (blue), HM (black) and SSE (red) methods, utilizing the φ directions from HIGeoCAT database are presented in the second row, and using the flare-site assumption in the third row, for STEREO-A (left) and STEREO-B (right) respectively.*

346

347   As described in section 2.3, we treat each event as a real-time case. We calculate the acceleration
348   (or deceleration) of the CME from a 2nd order polynomial fit (Equation 4) starting always from the
349   first three points and we are repeating the calculations adding one radial distance at a time up to
350   the last available point. The resulting kinematic curve for the August 4, 2011 CME, for ST-B and
351   the HM approximation using φ from flare site, is presented in Figure 2.
352
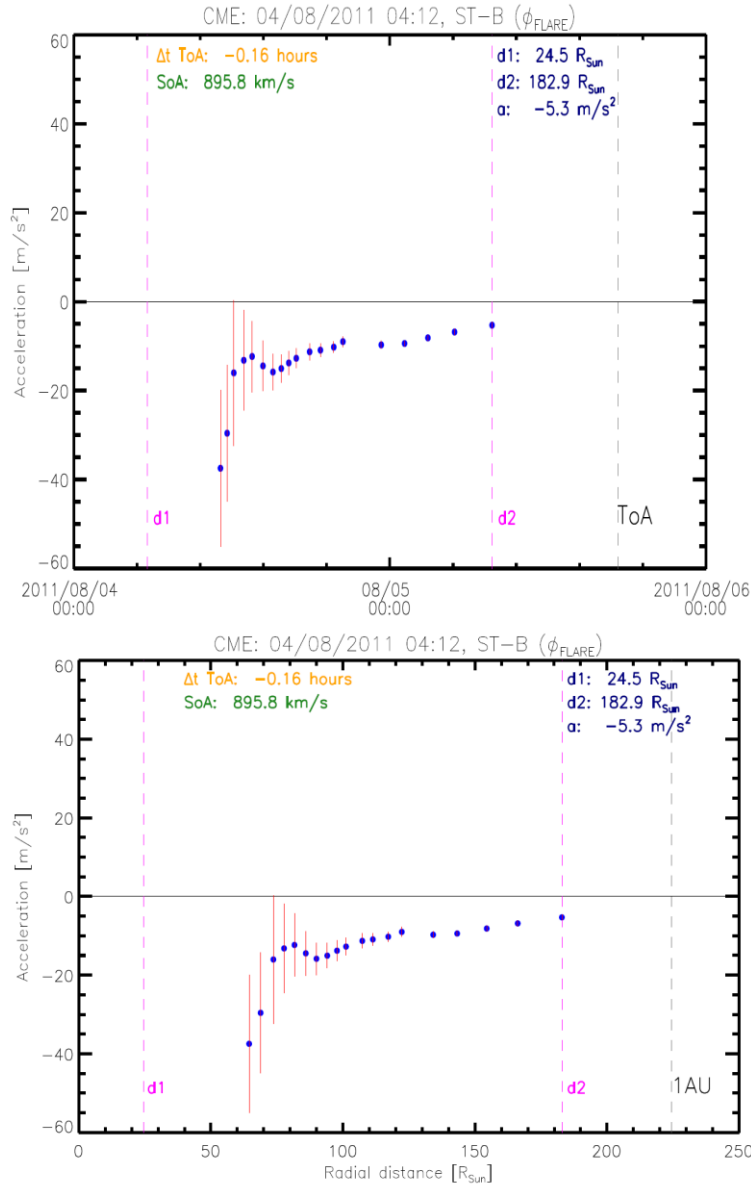
Figure 2. *The time-acceleration (top panel) and distance-acceleration (bottom panel) profiles for the August 04, 2011 CME using time-elongation data from ST-B, the HM approximation and φ from flare site. The deceleration phase lasts up to a distance of 182.9 Rs approximately (points within magenta dashed vertical lines) and then we assume that the ICME is moving with an almost constant speed. The two-phase kinematics approach gave a ToA error of -0.16 hours and a SoA of 895.8 km/s. The actual arrival time was 10 minutes later than our prediction and the maximum speed was about 700 km/s. The second vertical magenta dashed line indicates the transition from the deceleration phase to the movement with almost constant speed which*

minimizes the ToA error. The vertical grey dashed line corresponds to the actual arrival time of the ICME at 1 AU. The red vertical lines on each point indicates the calculated error for the acceleration.

353

354   The CME decelerates (*first phase*) from the first HI-1 observation, at a distance of $d_1 = 24.5$ Rs,
355   to the distance of $d_2 = 182.9$ Rs. We apply Eq. (4) on the available $r(t)$ points to obtain the
356   deceleration of 5.3 m/s^2. Beyond that distance we assume that the ICME is moving with constant
357   speed (*second phase*). The distance d_2 is obtained by minimizing the ToA error. The ToA error is
358   defined as $\Delta t = t_{predicted} - t_{observed}$. Ideally the selection of d_2 should lead to ToA error of 0. This
359   two-phase kinematics methodology estimates the arrival of the August 4, 2011 CME on August 5,
360   2011 at 17:10, which is 10 minutes earlier (i.e. -0.16 hours) than the actual arrival time. The
361   procedure of the two-phase kinematics which is the core of the HeRPA algorithm is presented
362   graphically in Figure 3. Furthermore, the estimated SoA was 896 km/s while the maximum
363   observed ICME speed (in the sheath) was 700 km/s. This analysis repeated also for the FP and
364   SSE approximations for ST-A and ST-B. The results for this ICME are presented in Table 2.
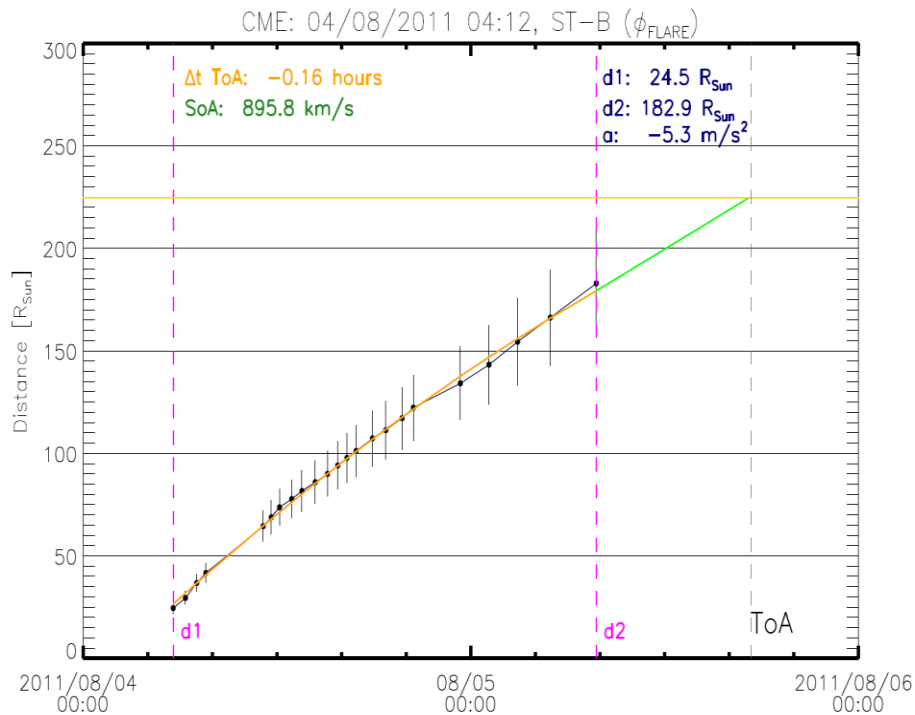
365

Figure 3. *An example of how HeRPA algorithm actually works for the August 4, 2011 CME. The radial distances as a function of time obtained from Eq. (2) utilizing φ from flare site for HM (black) approximation. The two vertical magenta dashed lines indicates the first phase of the deceleration of the ICME between d_1 (24.5 Rs) and d_2 (182.9 Rs) distances. The 2nd order polynomial fit (Eq. 4) applied on the available points and indicated with the orange curve. The second phase where the ICME is assumed to move with constant velocity from d_2 up to 1 AU is represented by the green straight line. Finally, the grey dashed vertical line represents the actual ToA of the ICME at Earth and the yellow horizontal line represents the calculated distance of 1 AU (in Rs).*

366
367

368

Table 2. *Estimated ToA errors (Δt) and SoA (V) for propagation directions from HIGeoCAT (φ_H) and the flare-site assumption (φ_F) for both spacecraft ST-A and ST-B for FP, HM and SSE approximations for the August 4, 2011 CME. The cases where unphysical accelerations and/or speeds-on-arrival occurred are indicated as failures (F) of the algorithm and does not take into account for the statistical analysis but we still provide the values for clarity.*

	φ_H (•)	Δt (hours)	V (km/s)	d_1 (Rs)	d_2 (Rs)	a (m/s²)	φ_F (•)	Δt (hours)	V (km/s)	d_1 (Rs)	d_2 (Rs)	a (m/s²)
	STEREO-A HI											
FP	109±2	-7.53	1332	16.9	57.2	-2.4	61.3±1	-0.32	1027	17.0	69.1	-8.1
HM	159±3	*-17.54 (F)*	*2024 (F)*	24.1	76.5	-0.5	61.3±1	0.18	1011	16.2	71.6	-8.4
SSE	131±2	-11.68	1549	19.2	59.4	-4.2	61.3±1	0.26	1006	16.5	71.7	-8.8
	STEREO-B HI											
FP	116±3	-9.70	1363	26.2	177.2	-4.2	131.9±2	*-19.39 (F)*	*2172 (F)*	33.1	97.5	-31.5
HM	170±4	*-20.98 (F)*	*2299 (F)*	38.2	174.5	-10.1	131.9±2	-0.16	896	24.5	182.9	-5.3
SSE	140±3	-12.77	1490	28.5	195.6	-5.5	131.9±2	-7.17	1179	26.0	166.3	-7.2

369

370   The results based on the HIGeoCAT directions (φ_H) overestimate of the event kinematics with
371 increased SoA speeds and early ToA predictions ranging between -8 and -13 hours. Furthermore,
372 the HM approximation fails, for both ST-A and ST-B, due to the large angles of 159° and 170°,
373 respectively. The flare-site assumption gives the best ToA results for both ST-A and ST-B. For
374 ST-A, the absolute ToA error is less than 20 minutes for all approximations. For ST-B the FP
375 approximation fails (F) as expected from the right plot of the third row of Figure 1 where the slope
376 of the blue points indicates a high SoA and as a result of an early prediction. The SSE
377 approximation gives an early prediction of -7 hours while the HM approximation gives the best
378 overall ToA prediction of just 10 minutes error. For this case, we obtain a SoA of almost 900 km/s
379 which is the closest value to the maximum observed speed of 700 km/s.
380   The first impression from this analysis is that the flare-site assumption appears to improve
381 significantly the ToA estimation with errors of the order of minutes. This is the first time, to the
382 best of our knowledge, where a methodology implementing HI observations and single-spacecraft
383 geometrical techniques, results in ToA errors below an hour.
384   A possible reason for the good ToA performance using the ST-A data with the flare-site
385 assumption is the elimination of the projection effects. In P21 we showed that projection effects
386 for CMEs associated with solar flares at longitudes beyond 60° are negligible, especially for CMEs
387 with true angular widths close to the upper limit of 94°. For this case study, the Spacecraft-Sun-
388 CME angle is 61.3°. Thus, the point tracked in the j-maps is likely the CME front (or a point close
389 to it). Furthermore, this CME has a true angular width of 107° according to the MVC catalogue
390 (Vourlidas et al., 2017) and this value is very close to our upper limit of 94° (P21).
391   On the other hand, the ST-B results, based on HIGeoCAT, are poorer. For the flare assumption,
392 the results are mixed: the FP approximation fails; the HM gives a good prediction; the SSE gives
393 an early prediction of 7 hours. In this case, φ = 131.9° and the CME is assumed to propagate away
394 from the ST-B in a direction where projection effects are important. Thus, it is possible the
395 assumed observed apex point to be actually a point in the flanks of the CME. This could also
396 explain why the HM approximation performs better in contrast to the other methods as the HM

397 direction in this case (for ST-B) is away from the radial direction of the flare (see Figure 1, top
398 row, right panel), so closer to the observed point (i.e. in the flanks and not at the assumed apex).
399

4 Results

401 We used STEREO/HI data to extract the kinematic profiles of 13 CMEs and derive their ToA and
402 the SoA at 1 AU. The FP, HM and SSE methods were applied in this work as single-spacecraft
403 geometric-fitting techniques to obtain the radial distances of the CME leading edge as a function
404 of time. When a CME was observed by both ST-A and ST-B it was treated as two independent
405 events. Taking this into consideration our sample of 13 CMEs/ICMEs consists of 21 independent
406 events.
407 All the information from our analysis is provided as a supplementary material. For each case we
408 provide: the date and time of the onset of the CME from LASCO coronagraphs, the φ angle (from
409 HIGeoCAT and the flare-site assumption), the ToA error (in hours), the SoA (in km/s), the
410 distances d_1 and d_2 (in solar radii), and finally, the acceleration (or deceleration).
411 We calculate for each case basic statistical metrics which have been used also previous published
412 works for the issue of the ToA (see e.g. Riley et al., 2018; Verbeke et al., 2019; Paouris et al.,
413 2021a; P21). These metrics are the median, the mean error (ME), the mean absolute error (MAE)
414 and the root mean square error (RMSE). All the metrics for each case utilizing φ angles from the
415 HIGeoCAT catalogue as well as from the flare site are presented in Table 3. The standard errors
416 are calculated by a simple bootstrap method with replacement for 10^6 runs.
417 The analysis revealed several interesting results. Unsurprisingly, perhaps, the assumption of
418 deceleration (or acceleration) is a better representation of the real CME kinematics in the inner
419 heliosphere as suggested by the improved MAE values. For example, using the same geometric
420 technique (SSE), the HeRPA-based ToA predictions show an improvement of almost 3.5 hours
421 against the ARRCAT predictions, which are made under the assumptions of constant direction and
422 speed.
423

Table 3. *Basic statistical metrics for ToA (in hours) for each geometrical technique utilizing the φ angle from HIGeoCAT and flare-site assumption (last two columns). For comparison we also present the metrics for ToA using the predicted arrival times from ARRCAT (third column) under the assumption of constant speed movement with the SSE approximation.*

		ARRCAT	φ from HIGeoCAT	φ from FLARE site
Median	*FP*	-	**-1.0±2.5**	-7.3±6.0
	HM	-	-12.7±5.2	**-0.3±2.7**
	SSE	-2.1±5.7	-5.8±3.5	-0.9±4.1
Mean Error (ME)	*FP*	-	**-4.7±2.1**	-10.5±3.4
	HM	-	-11.2±2.9	**-5.7±2.1**
	SSE	-3.6±5.0	-6.8±2.2	-6.8±2.4
Mean Absolute Error (MAE)	*FP*	-	**6.9±1.8**	11.1±3.2
	HM	-	13.0±2.4	**6.4±1.9**
	SSE	11.5±3.4	9.0±1.7	8.1±2.1
Root Mean Square Error (RMSE)	*FP*	-	**10.4±2.0**	16.1±3.2
	HM	-	16.4±2.4	**10.6±2.2**
	SSE	14.9±3.5	11.7±1.8	12.2±2.2

424

425 Furthermore, we see that our method tends to early predictions (see also Figure 4), i.e. the ICME
426 arrived later than the predicted ToA for all cases, resulting from the overestimation of the radial
427 distance, which leads to higher accelerations and/or higher speeds-on-arrival and hence to early
428 arrivals. When the φ propagation directions used by HIGeoCAT we see a much better performance
429 for FP approximation (MAE of 6.9±1.8 hours), while for the φ directions from the associated flare
430 site we see the best overall performance for HM approximation with an MAE of 6.4±1.9 hours.
431
432 We can understand the difference in the performance by considering the propagation directions of
433 the 21 cases for the FP, HM and SSE methods relative to the spacecraft. One should always keep
434 in mind that we use geometric techniques so, it is very important to take also into account the
435 positions of ST-A and ST-B spacecraft for each case. The mean angular separation from all events
436 for the FP, HM and SSE methods is $<\varphi_{FP}> = 88.1°$, $<\varphi_{SSE}> = 103.4°$ and $<\varphi_{HM}> = 120.7°$,
437 respectively, when using the HIGeoCAT φ angles and the mean $<\varphi>$ utilizing the flare-site
438 assumption is 108.1°. Taking into account that in Equations (1) – (3) we can see that the sum $(a+\varphi)$
439 can to reach angles close to the critical angles (as described in section 2.3) for the SSE and HM
440 approximations in HIGeoCAT leading to unphysical results. This is the reason we see more
441 failures of our algorithm for FP approximation when the φ from flare site is used, the percentage
442 of the failures raised from 9.5% (HIGeoCAT) to 38.1 % (flare-site). This logic explains the
443 decrease of the failures for HM from 19.0% (HIGeoCAT) to 9.5% (flare-site). From our point of
444 view, the angles above explain two important observations: (1) the better performance of the FP
445 approximation, in contrast to HM and SSE, when using the HIGeoCAT angles, and (2), the
446 improvement in the results from HM and SSE when the φ direction is obtained from the associated
447 solar flare.
448 The propagation direction from the flare site offers the best overall performance. After we exclude
449 the cases with unphysical accelerations and velocities, due to the projection effects or the critical
450 angles, the remaining 50 predictions from all of the geometric techniques (FP, HM and SSE) result
451 in absolute ToA errors below 5 hours in 28 cases (56%). In only 8 cases (16%) we get absolute
452 errors greater than 20 hours. Figure 4 shows the error distribution for all successful cases for φ
453 from HIGeoCAT (top panel) as well as φ from flare site (bottom panel). If we focus on the cases
454 where the absolute errors are below 5 hours, as these cases are more important from space weather
455 point of view, we clearly see the superior performance of our HeRPA algorithm while for φ from
456 flare site, 21 cases has absolute errors less than 52 minutes (inset in the Figure 4 bottom panel).
457 For 17 of these events, the best performance comes from the HM and SSE approximations.
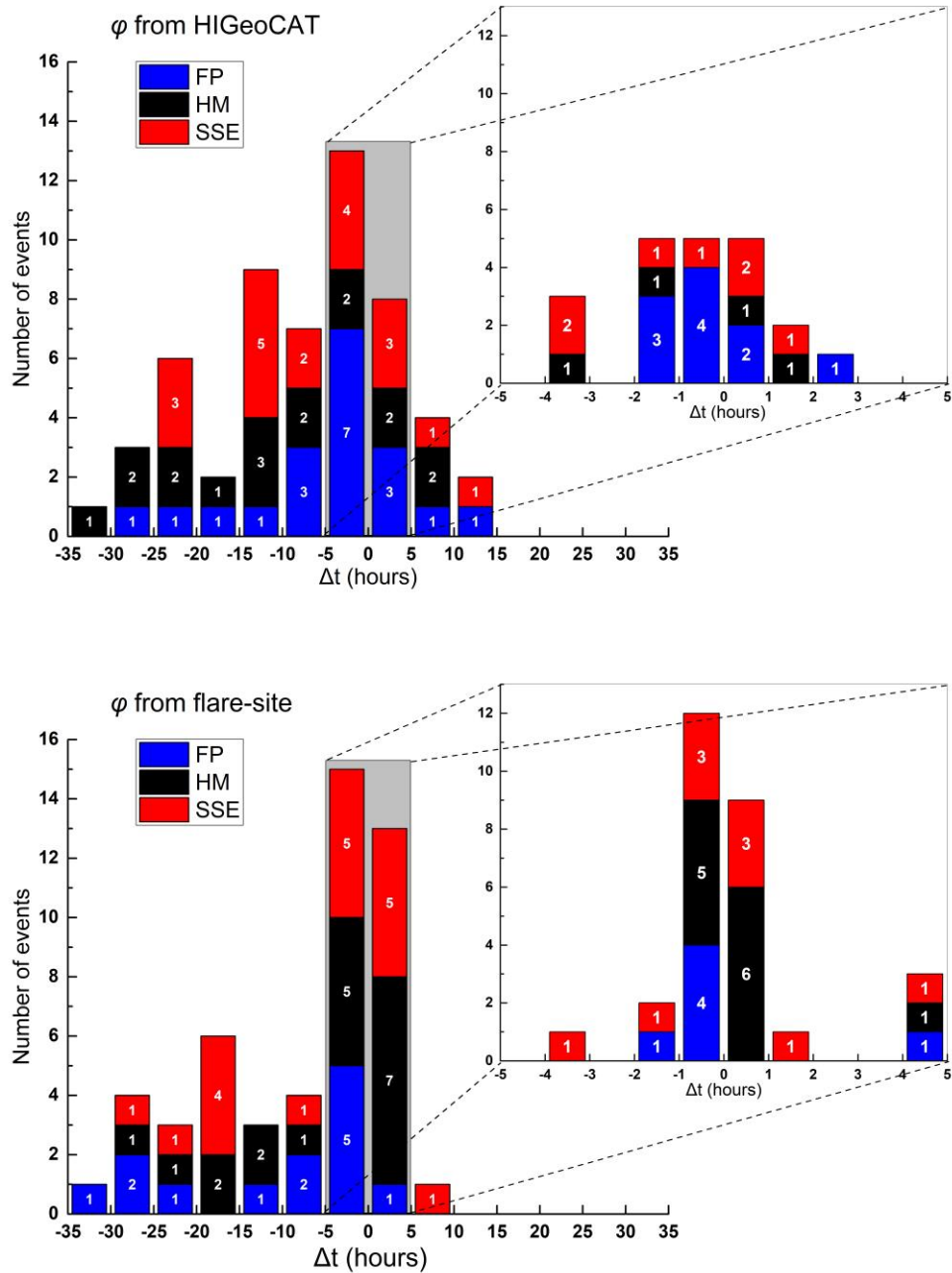458

Figure 4. *Difference between prediction and observed arrival times (Δt) and their distributions of a bin of 5 hours for the 55 successful applications of our algorithm for HIGeoCAT (top panel) and 50 for flare-site (bottom panel). The geometric techniques of FP, HM and SSE are indicating with blue, black and red colors. The superior performance of our algorithm when the φ direction is obtained from the flare site (bottom panel) is obvious. In particular, 28 (56%) of these events have an absolute error < 5 hours with 21 of those having an absolute error Δt < 52 minutes. For the same range of error < 5 hours for HIGeoCAT (top panel) we see a wider distribution without any remarkable performance.*

460 Our algorithm is motivated by the need for a near real-time tool to exploit HI data from off Sun-
461 Earth line viewpoints, such as the likely ESA mission to L5 (Pulikinnen et al., 2019). The L5
462 mission provides the unique opportunity to observe Earth-directed ICMEs from an observer angle
463 of 60° with respect to Sun-Earth line where the projection effects are negligible for these events,
464 as we showed in P21.
465 If we focus on the events where the SC_{angle} is less than 95° then our methodology provides good
466 results for a "wider" L5 scenario. This is the first time where the MAE is less than 1 hour
467 (0.96±0.52 hours for HM) for a small sample of 7 events of a total of 21 where the SC_{angle} ranges
468 between 57° and 95°. The direct comparison of all the statistical metrics are indicating that HeRPA
469 algorithm gives very good results if the flare-site assumption is used. In particular, there are two
470 cases with SC_{angle} very close to the ideal angle of L5 scenario (i.e. 57° and 67° respectively) where
471 the Δt in both cases is less than 50 minutes. The above analysis shows the potential for accurate
472 space weather forecasts, in terms of ToA, of a future L5 mission. The statistical metrics are
473 presented in Table 4.
474

Table 4. *Basic statistical metrics for ToA (in hours) for each geometrical technique utilizing the φ angle from HIGeoCAT and flare-site assumption for events with spacecraft's separation angle with Earth less than 95°.*

		φ from HIGeoCAT	**φ from FLARE site**
Median	*FP*	**-1.04±2.86**	-0.51±1.41
	HM	-2.47±3.32	**-0.16±0.52**
	SSE	-3.22±3.56	-0.41±0.91
Mean Error (ME)	*FP*	**-2.06±1.96**	-1.07±1.44
	HM	-2.96±2.48	**+0.46±0.61**
	SSE	-3.55±2.27	-0.66±1.18
Mean Absolute Error (MAE)	*FP*	**3.95±1.49**	2.45±1.12
	HM	5.24±1.74	**0.96±0.52**
	SSE	5.56±1.59	1.99±0.94
Root Mean Square Error (RMSE)	*FP*	**5.58±1.46**	3.68±1.31
	HM	6.75±1.96	**1.68±0.80**
	SSE	6.98±1.60	3.19±1.18

475

5 Discussion and Conclusions

476
477 In this work we investigated the reliability of the transformation of elongation angles to radial
478 distances under only the assumption of constant propagation direction. We treated the CME speed
479 as variable, in contrast to previous works (Sheeley et al., 1999; 2008; Kahler and Webb, 2007;
480 Rouillard et al., 2008; Lugaz et al., 2009; Lugaz et al., 2010; Davies et al., 2012; Barnes et al.,
481 2019; Möstl et al., 2011; Möstl and Davies, 2013; Möstl et al., 2014) which also used single
482 spacecraft geometric techniques. We find considerable improvement in the prediction of the arrival
483 time of the CMEs by taking into consideration their deceleration in the interplanetary space and
484 the location of the source region in contrast to previous methodologies based on constant direction
485 and speed. A sample of 13 CMEs/ICMEs analyzed independently for ST-A and/or ST-B
486 observations resulted in a set of 21 unique CME/ICME events with a mixture of slow and fast
487 CMEs. This mix allowed us to test our method across a rather representative CME sample.

488 For each CME, we compare our results using two different values for the propagation direction;
489 the angles provided by the HIGeoCAT catalogue and the angle resulting from the assumption of
490 radial propagation from the flare site. Then, for each propagation direction, we transform
491 elongation to radial distance, directly from the equations (1)-(3) for the FP, HM and SSE
492 approximations, respectively.

493 Finally, we fit the resulting distance-time data with a two-phase kinematic profile (CME
494 accelerating or decelerating, up to a distance d_1, then coasting to 1 AU with constant speed). We
495 simulate a data-assimilation scenario where HI measurements are added in time, as the event
496 progresses, by starting the fitting procedure with the first three measurements and updating the fit
497 one measurement at a time until the last available HI measurement. For each point, we make a
498 prediction for the ToA and SoA at Earth.

499 The first finding from our analysis is that a variable CME speed (along a constant propagation
500 direction) leads to better ToA estimates. Our assumed two-phase kinematic profile is consistent
501 with past findings (Wood et al. 2017; Sachdeva et al. 2017; Colaninno et al. 2013) that indicate
502 that CMEs continue to evolve beyond the typical coronagraph fields of view (i.e., beyond 15-30
503 Rs). Hence, heliospheric imaging observations are of considerable value in future space weather
504 observing architectures.

505 We should not lose sight of the fact, however, that CME speed and direction are highly coupled
506 the methodologies discussed here. They cannot be decoupled with single viewpoint observations
507 or even dual viewpoint ones, as projection effects become quite important when dealing with the
508 long lines-of-sight through the CMEs at these heliocentric distances. This issue seems partially
509 responsible for the poorer performance when HIGeoCAT propagation directions are used. The
510 directions are derived under the assumptions of both constant speed and direction for the CME
511 apex. However, it has been shown (e.g., Liewer et al. 2011; Colaninno et al. 2013) that as the CME
512 expands, projection effects tend to move the (projected) apex to the flanks of the event. This
513 apparent motion registers as a deceleration that will couple into a direction/speed bias when both
514 of these quantities are held constant. o

515 Our second finding is that the flare-site assumption provides better ToA estimates than the
516 HIGeoCAT φ directions, with an MAE of 6.4±1.9 hours. This can be seen in Figure 4 where 21
517 cases have an ToA error below 52 minutes. Figure 5 shows the effectiveness of the flare-site
518 assumption from a geometrical point of view. The ToA error for the flare-site based HM and SSE
519 approximations lie close to $\Delta t = 0$ when the SC_{angle} is less than 100°. These statistics are
520 encouraging for our 'real-time' approach since the HeRPA algorithm can be applied soon after the
521 first three HI images are obtained (assuming, of course, that an associated solar flare is detected
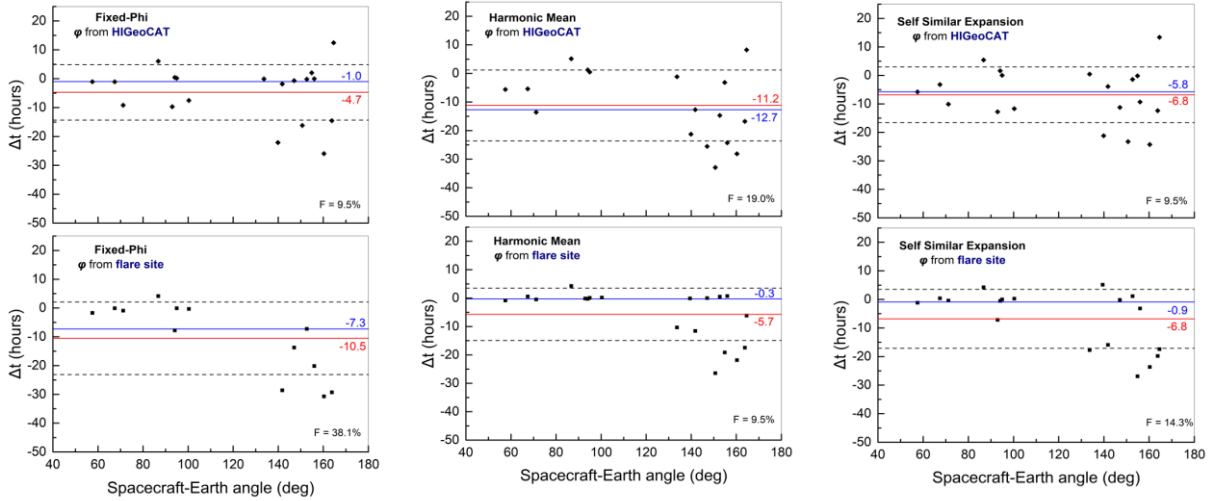522 from the Sun-Earth line).

523
524
525

Figure 5. *Difference between prediction and observed arrival times (Δt) as a function of the spacecraft angle (SC_angle) with respect to Sun-Earth line for FP (left panels), HM (middle panels) and SSE (right panels) approximations utilizing φ directions from HIGeoCAT (top row panels) and from flare-site assumption (bottom row panels). It is obvious that for SC_angle < 100° the majority of the points are lying on the line Δt=0 indicating almost an ideal performance of our algorithm especially for the HM and SSE approximations when the φ angle is utilized by the flare-site assumption in contrast to the φ from HIGeoCAT. For SC_angle > 130° the points are scattered as it was expected due to the importance of the projection effects. At the bottom right corner in every plot the percentage of the failures of our algorithm is also presented.*

526

527 Finally, our methodology allowed us to compare the lead time of the ToA prediction against the
528 ToA error. We show that relationship for 11 cases of the HM approximation, which has an absolute
529 error Δt of less than 1 hour (Figure 6). We study also the CME distance when the prediction is
530 made against the error, to provide a sense of the location of the CME in the inner heliosphere. We
531 see that the ToA accuracy varies considerably from case to case. Only a handful of cases show a
532 reduction of the error with decreasing lead time, which would correspond to the expected trend for
533 the ideal case. All cases start with considerable overpredictions (negative Δt) indicating that the
534 speed derived from the earlier measurements are too high, therefore CMEs decelerate considerably
535 in the HI FOVs. This trend is reversed, for most cases, as more measurements become available
536 but the error remains within 10 hours, with the exception of cases 04/08/2011 ST-A and
537 29/09/2013 ST-A. The underprediction points to projection effects discussed earlier. It appears
538 that, at larger elongations, the observer follows a point on the CME front that it is not directed at
539 Earth. This is particularly obvious for 04/08/2011 ST-A where according to the measurements the
540 event is at 150 Rs but the CME has actually arrived at Earth. Clearly, we will be unable to make
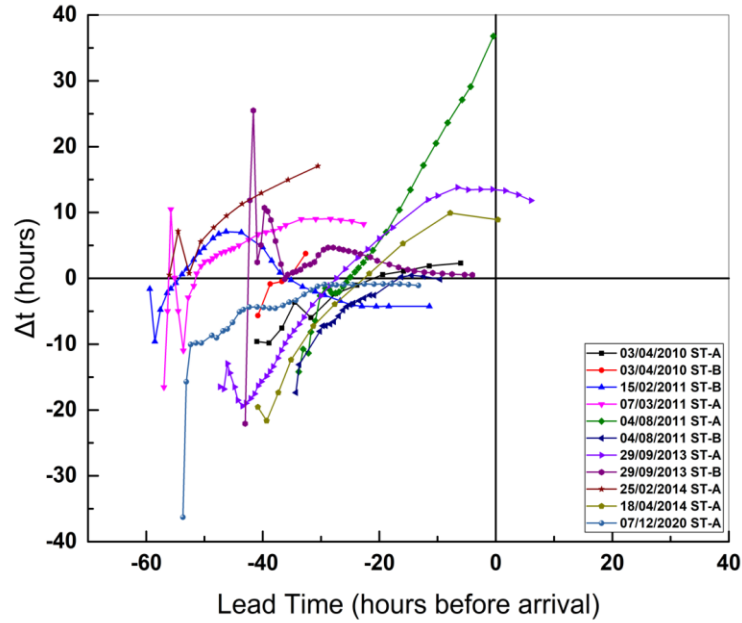541 concrete advances in ToA accuracy without first reigning in projection effects at large elongation.

Figure 6. *Time-of-Arrival error vs. lead prediction time in hours before arrival for 11 cases of HM approximation utilizing the flare site assumption. These events have all a best ToA error less than 1 hour.*

542

543 One way to test the reliability of the explanation provided above is through the attempt to minimize
544 the projection effects. The projection effects depend on the direction of the CME relative to the
545 observer. The best way to minimize projection effects is to observe a CME in quadrature or, at
546 least, from angles above 60° (see P21).
547 We examine the December 7, 2020 CME. The CME is associated with a C7.4 class solar flare
548 erupted from AR12790 at 16:32 peak time, with heliographic coordinates S23W11. The
549 perspective of ST-A is ideal for this case, as the spacecraft observes from an angle of about 68.5°,
550 assuming that the CME is propagating radially from the flare site. Using the flare-site assumption,
551 we obtain good ToA estimates for all three geometric techniques. The best ToA arises from the
552 HM approximation which predicts 50 minutes earlier arrival. The SoA is 634 km/s compared to
553 the observed speed of 493 km/s. Looking at Figure 7, we see that the angle from the HIGeoCAT
554 FP approximation is closely aligned to the flare site direction with the other directions less than
555 20° to the west. So, we would expect that HIGeoCAT-based prediction will provide similar levels
556 of accuracy. Indeed, the HIGeoCAT FP approximation error is -1.04 hours. However, the other
557 two approximations result in -5.6h (HM) and -5.8h (SSE) with SoA of 715 and 723 km/s,
558 respectively. Clearly, the HIGeoCAT-based directions underperform the flare-site approximation
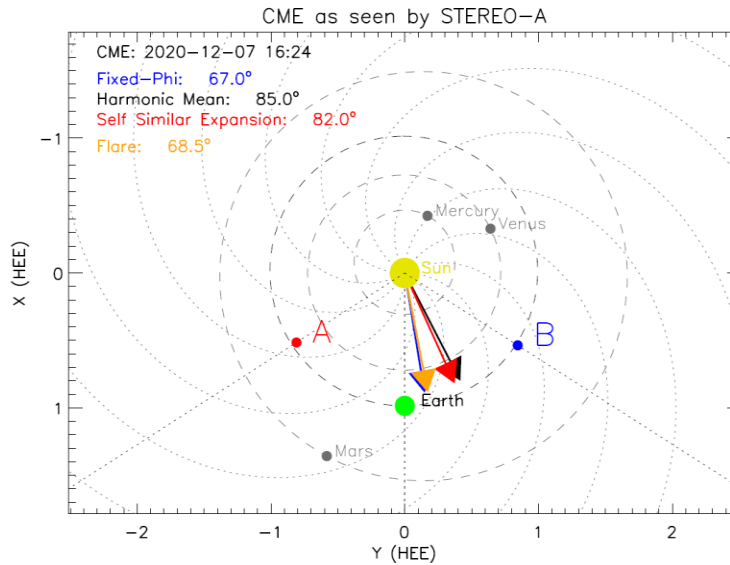559 across the three techniques considered here.
560

Figure 7. *Propagation directions (φ) for December 7, 2020 CME for FP (blue), HM (black) and SSE (red) approximations for STEREO-A. The radial direction of the associated C7.4 solar flare is also indicated (orange arrow).*

561

562 A way to validate our flare-site assumption is to compare the flare-based propagation angle φ
563 against the same angle derived by a multiview triangulation technique. Several such techniques
564 exist and are based on the assumption that either both ST-A and ST-B track the same point of the
565 CME front (e.g. Liu et al., 2010a; Liu et al., 2010b) or that they track different points on the tangent
566 of a circular CME cross section anchored the Sun (Lugaz et al., 2010). We use the harmonic mean
567 triangulation (HMT) technique presented in Lugaz et al., 2010 as it seems more realistic.
568 Unfortunately, the technique has its limitations and only one of the events in our list (out of eight
569 possible) resulted in reasonable ToA. In particular, five cases occur when the STEREO spacecraft
570 are beyond 120 deg from Earth. In these extreme viewing conditions, the fundamental assumption
571 of Lugaz et al., 2010 that the tracking points lie on the tangent of the CME envelope may break
572 down. The two spacecraft are almost surely tracking the opposite sides of CME flanks which may
573 propagate independently at these distances. In another two cases, the ST-A and -B spacecraft are
574 in opposition and hence provide symmetric views of Earth-directed events. In this situation, the
575 two views reduce to a single view effectively and the triangulation provides unreliable results. We
576 are left with triangulation results for the April 3, 2010 CME only. The direction from the HMT is
577 -13.6°±2.9° while the longitude of the associated solar flare is +3°. The CME direction as it is
578 calculated with the HMT technique results to a reasonable angle close to our flare-site assumption.
579 This provides further support that the flare-site assumption may be a better representation of the
580 CME direction than the single viewpoint derived directions from HIGeoCAT.
581 Concluding, our methodology offers a new way to assess the ToA issue using data from
582 heliospheric imagers. HeRPA algorithm is able, in principle, to perform the ToA analysis as soon
583 data become available. This approach should be useful for operational spacecraft at the Lagrange
584 points. Finally, we hope that such a service will be useful for space weather forecasting purposes
585 in addition to the safety precautionary measures for manned space missions to Moon and Mars.

586 **Acknowledgments**

596

597 **Appendix I**
598 **Interpretation of elongation angles**
599 The elongation angle, and eventually radial distance depends on the propagation angle φ in
600 different ways for the three approximations. So, the same propagation angle φ could result in very
601 different distance estimates. We proceed by rewriting the equations (1) – (3) with elongation angle
602 a expressed as a function of the dimensionless parameter $\rho = r/d_{SC}$, where r is the radial distance
603 and d_{SC} is the spacecraft-Sun distance. The equations for FP, HM and SSE are:

$$a_{FP} = \frac{\sin\varphi_{FP}}{1 - \cos\varphi_{FP}} \quad (6)$$

$$a_{HM} = \cos^{-1}\left(\frac{b_1 \cdot \sqrt{b_1^2 + b_2^2 - 1} - b_2}{b_1^2 + b_2^2} \right) \quad (7)$$

606 where $b_1 = 2.0/\rho - \cos(\varphi_{HM})$ and $b_2 = \sin(\varphi_{HM})$ and,

$$a_{SSE} = \cos^{-1}\left(\frac{c_1 \cdot \sqrt{c_1^2 + c_2^2 - c_3^2} - c_2 \cdot c_3}{c_1^2 + c_2^2} \right) \quad (8)$$

608 where $c_1 = [(1.0 + c_3)/\rho] - \cos(\varphi_{SSE})$, $c_2 = \sin(\varphi_{SSE})$ and $c_3 = \sin\lambda$. In our analysis λ is equal to 33.75°
609 for all cases (see section 2.3). The elongation angle as a function of the dimensionless parameter
610 $\rho = r/d_{SC}$ is plotted in the next figure for φ of 30°, 60°, 90°, 120° and 150.
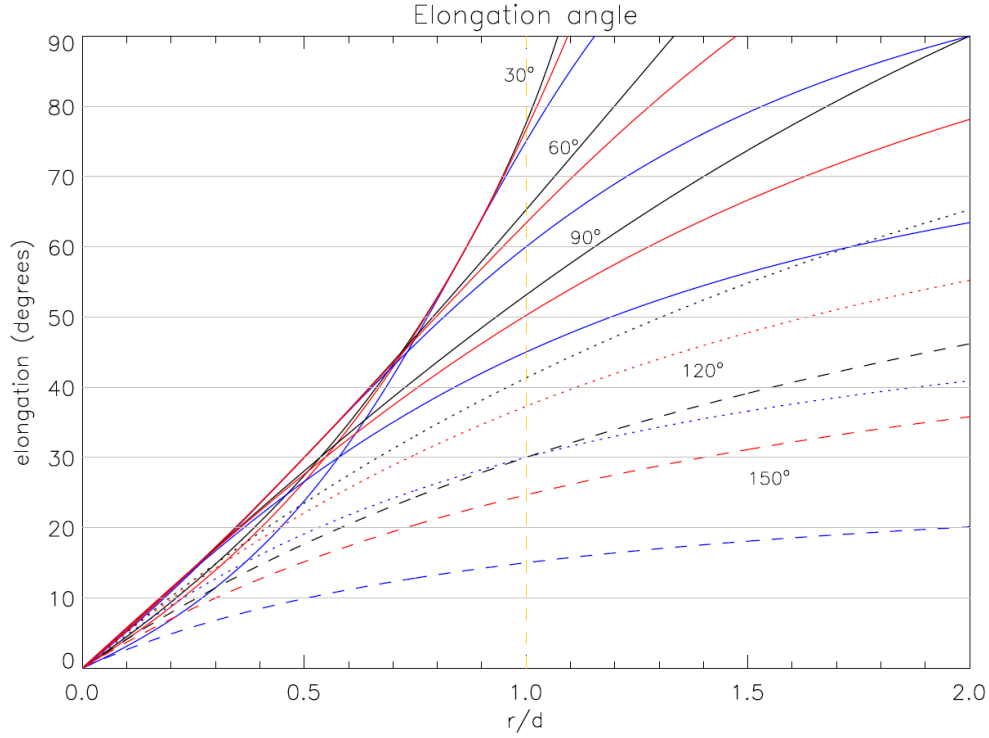
611

Figure 8. *Elongation angle as a function of the dimensionless parameter r/d$_{SC}$ for FP (blue), HM (black) and SSE (red) approximations for five different propagation direction angles φ of 30°, 60°, 90°, 120° and 150°. The vertical orange dashed line indicates the 1 AU distance. The curves of 120° and 150° are represented with dots and dashes for better visual identification.*

612

613   We focus on the consistency of the 1 AU distance as derived by the three approximations. For
614   relatively small φ angles (e.g., 30° or 60°), the distance of 1 AU has small differences for the
615   elongation angles among the FP, HM and SSE approximations. For larger φ angles the distance
616   of 1 AU has much larger differences between the FP, HM and SSE methods. In particular, for φ
617   of 120° (dotted curves in Figure 8) we take an 1 AU correspondence elongation angle of 30° for
618   FP, 41.3° for HM, and 37.3° for SSE. Plots similar to our Figure 8 presented also by Sheeley et
619   al., 2008; Lugaz, 2010 and Davies et al., 2012. Sheeley et al., 2008 plotted the elongation angles
620   as a function of the dimensionless parameter ρ. Lugaz, 2010 plotted the elongation angles as a
621   function of time, since CME launch, for FP and HM methods assuming a constant transient
622   speed of 400 km/s and a fixed distance of 0.975 AU. Davies et al., 2012 plotted the elongation
623   angles as a function of time (since CME launch) for FP, HM and SSE methods assuming a
624   movement with a constant speed of 400 km/s.
625
626
627
628
629
630
631
632

References

Balmaceda, L. A., Vourlidas, A., Stenborg, G., & Dal Lago, A. (2018). How reliable are the properties of coronal mass ejections measured from a single viewpoint?, The Astrophysical Journal, 863, 57. https://doi.org/10.3847/1538-4357/aacff8

Barnes, D., Davies, J.A., Harrison, R.A. et al. CMEs in the Heliosphere: II. A Statistical Analysis of the Kinematic Properties Derived from Single-Spacecraft Geometrical Modelling Techniques Applied to CMEs Detected in the Heliosphere from 2007 to 2017 by STEREO/HI-1. Sol Phys 294, 57 (2019). https://doi.org/10.1007/s11207-019-1444-4

Brueckner, G. E., Howard, R. A., Koomen, M. J., Korendyke, C. M., Michels, D. J., Moses, J. D., et al. (1995). The large angle spectroscopic coronagraph (LASCO). Solar Physics, 162, 357–402. https://doi.org/10.1007/BF00733434

Byrne, J.P. et al. Propagation of an Earth-directed coronal mass ejection in three dimensions. (2010) Nat. Commun. 1:74 DOI: https://doi.org/10.1038/ncomms1077

Čalogović, J., Dumbović, M., Sudar, D. et al. Probabilistic Drag-Based Ensemble Model (DBEM) Evaluation for Heliospheric Propagation of CMEs. Sol Phys 296, 114 (2021). https://doi.org/10.1007/s11207-021-01859-5

Cohen, O., G. D. R. Attrill, N. A. Schwadron, N. U. Crooker, M. J. Owens, C. Downs, and T. I. Gombosi (2010), Numerical simulation of the 12 May 1997 CME Event: The role of magnetic reconnection, J. Geophys. Res., 115, A10104, DOI: https://doi.org/10.1029/2010JA015464

Colaninno, R. C., Vourlidas, A., & Wu, C. C. (2013). Quantitative comparison of methods for predicting the arrival of coronal mass ejections at Earth based on multiview imaging. Journal of Geophysical Research: Space Physics, 118(11), 6866-6879. DOI: https://doi.org/10.1002/2013JA019205

Davies, J. A., Harrison, R. A., Perry, C. H., Möstl, C., Lugaz, N., Rollett, T., ... & Savani, N. P. (2012). A self-similar expansion model for use in solar wind transient propagation studies. The Astrophysical Journal, 750(1), 23. DOI: https://doi.org/10.1088/0004-637X/750/1/23

Domingo, V., Fleck, B., & Poland, A. I. (1995). The SOHO mission: An overview. Solar Physics, 162, 1–37. https://doi.org/10.1007/BF00733425

Dumbovic, M., Calogovic, J., Vrsnak, B., Temmer, M., Mays, M.L., Veronig, A., Piantschitsch, I.: 2018, Astrophys. J. 854, 180. DOI: https://doi.org/10.3847/1538-4357/aaaa66

Eyles, C. J., et al. "The heliospheric imagers onboard the STEREO mission." Solar Physics 254, 2 (2009): 387-445. DOI: https://doi.org/10.1007/s11207-008-9299-0

Gopalswamy, N., Lara, A., Yashiro, S., Kaiser, M.L., Howard, R.A.: 2001, J. Geophys. Res. 106(29), 207. DOI: https://doi.org/10.1029/2001JA000177

678

679 Howard, R.A., Moses, J.D., Vourlidas, A. et al. Sun Earth Connection Coronal and Heliospheric

680 Investigation (SECCHI). Space Sci Rev 136, 67 (2008). https://doi.org/10.1007/s11214-008-

681 9341-4

682

683 Howard, T. A., & Tappin, S. J. (2008). Three-dimensional reconstruction of two solar coronal

684 mass ejections using the STEREO spacecraft. Solar Physics, 252, 373.

685 https://doi.org/10.1007/s11207-008-9262-0

686

687 Isavnin, A., Vourlidas, A., & Kilpua, E. K. J. (2013). Three-dimensional evolution of erupted

688 flux ropes from the Sun (2–20 R$\odot$) to 1 AU. Solar Physics, 284(1), 203-215. DOI:

689 https://doi.org/10.1007/s11207-012-0214-3

690

691 Jang, S., Moon, Y. J., Kim, R. S., Lee, H., & Cho, K. S. (2016). Comparison between 2D and 3D

692 parameters of 306 front-side halo CMEs from 2009 to 2013. The Astrophysical Journal, 821, 95.

693 https://doi.org/10.3847/0004-637X/821/2/95

694

695 Kahler, S. W., & Webb, D. F. (2007). V arc interplanetary coronal mass ejections observed with

696 the Solar Mass Ejection Imager. Journal of Geophysical Research: Space Physics, 112(A9).

697 Kaiser, M. L., Kucera, T. A., Davila, J. M., Cyr, St.O. C., Guhathakurta, M., & Christian, E.

698 (2008). The STEREO mission: An introduction. Space Science Reviews, 136, 5–16.

699 https://doi.org/10.1007/s11214-007-9277-0

700

701 Kay, C., Opher, M., & Evans, R. M. (2013). Forecasting a coronal mass ejection's altered

702 trajectory: ForeCAT. The Astrophysical Journal, 775(1), 5. DOI: https://doi.org/10.1088/0004-

703 637X/775/1/5

704

705 Kay, C., M. Opher, and R. M. Evans. "Global trends of CME deflections based on CME and

706 solar parameters." The Astrophysical Journal 805.2 (2015): 168. DOI:

707 https://doi.org/10.1088/0004-637X/805/2/168

708

709 Lee, H., Moon, Y. J., Na, H., Jang, S., & Lee, J. O. (2015). Are 3-D coronal mass ejection

710 parameters from single-view observations consistent with multi view ones?. Journal of

711 Geophysical Research: Space Physics, 120, 10237–10249.

712 https://doi.org/10.1002/2015JA021118

713

714 Liewer, P. C., Hall, J. R., Howard, R. A., De Jong, E. M., Thompson, W. T., & Thernisien, A.

715 (2011). Stereoscopic analysis of STEREO/SECCHI data for CME trajectory determination.

716 Journal of atmospheric and solar-terrestrial physics, 73(10), 1173-1186. DOI:

717 https://doi.org/10.1016/j.jastp.2010.09.004

718

719 Liu, Y., Davies, J. A., Luhmann, J. G., Vourlidas, A., Bale, S. D., & Lin, R. P. (2010a).

720 Geometric triangulation of imaging observations to track coronal mass ejections continuously

721 out to 1 AU. The Astrophysical Journal Letters, 710(1), L82. DOI: https://doi.org/10.1088/2041-

722 8205/710/1/L82

723

Liu, Y., Thernisien, A., Luhmann, J. G., Vourlidas, A., Davies, J. A., Lin, R. P., & Bale, S. D. (2010b). Reconstructing coronal mass ejections with coordinated imaging and in situ observations: Global structure, kinematics, and implications for space weather forecasting. The Astrophysical Journal, 722(2), 1762. DOI: https://doi.org/10.1088/0004-637X/722/2/1762

Liu, Y. D., Luhmann, J. G., Lugaz, N., Möstl, C., Davies, J. A., Bale, S. D., & Lin, R. P. (2013). On Sun-to-Earth propagation of coronal mass ejections. The Astrophysical Journal, 769, 45. DOI: https://doi.org/10.1088/0004-637X/769/1/45

Lugaz, N. (2010). Accuracy and limitations of fitting and stereoscopic methods to determine the direction of coronal mass ejections from heliospheric imagers observations. Solar Physics, 267(2), 411-429. DOI: https://doi.org/10.1007/s11207-010-9654-9

Lugaz, N., Vourlidas, A., & Roussev, I. I. (2009, September). Deriving the radial distances of wide coronal mass ejections from elongation measurements in the heliosphere–application to CME-CME interaction. In Annales Geophysicae (Vol. 27, No. 9, pp. 3479-3488). Copernicus GmbH. DOI: https://doi.org/10.5194/angeo-27-3479-2009

Lugaz, N., Hernandez-Charpak, J. N., Roussev, I. I., Davis, C. J., Vourlidas, A., & Davies, J. A. (2010). Determining the azimuthal properties of coronal mass ejections from multi-spacecraft remote-sensing observations with STEREO SECCHI. The Astrophysical Journal, 715(1), 493. DOI: https://doi.org/10.1088/0004-637X/715/1/493

Lugaz, N., Farrugia, C. J., Davies, J. A., Möstl, C., Davis, C. J., Roussev, I. I., & Temmer, M. (2012). The deflection of the two interacting coronal mass ejections of 2010 May 23–24 as revealed by combined in situ measurements and heliospheric imaging. The Astrophysical Journal, 759(1), 68. DOI: https://doi.org/10.1088/0004-637X/759/1/68

Lynch, B.J., Antiochos, S.K., Li, Y., Luhmann, J.G., DeVore, C.R.: 2009, Rotation of coronal mass ejections during eruption. Astrophys. J. 697, 1918. DOI: https://doi.org/10.1088/0004-637X/697/2/1918.

Manoharan, P. K., Tokumaru, M., Pick, M., Subramanian, P., Ipavich, F. M., Schenk, K., ... & Vourlidas, A. (2001). Coronal mass ejection of 2000 July 14 flare event: Imaging from near-Sun to Earth environment. The Astrophysical Journal, 559(2), 1180. DOI: https://doi.org/10.1086/322332

Mays, M.L., Taktakishvili, A., Pulkkinen, A. et al. Ensemble Modeling of CMEs Using the WSA–ENLIL+Cone Model. Sol Phys 290, 1775–1814 (2015). https://doi.org/10.1007/s11207-015-0692-1

Mierla, M., Davila, J., Thompson, W., Inhester, B., Srivastava, N., Kramar, M., et al. (2008). A quick method for estimating the propagation direction of coronal mass ejections using STEREO-COR1 images. Solar Physics, 252, 385–396. https://doi.org/10.1007/s11207-008-9267-8

Möstl, C., & Davies, J. A. (2013). Speeds and arrival times of solar transients approximated by self-similar expanding circular fronts. Solar Physics, 285(1), 411-423. DOI: https://doi.org/10.1007/s11207-012-9978-8

Möstl, C., Amla, K., Hall, J.R., Liewer, P.C., De Jong, E.M., Colaninno, R.C., Veronig, A.M., Rollett, T., Temmer, M., et al., (2014), Connecting Speeds, Directions and Arrival Times of 22 Coronal Mass Ejections from the Sun to 1 AU. The Astrophysical Journal, 787, 119. DOI: https://doi.org/10.1088/0004-637X/787/2/119

Möstl, C., Rollett, T., Lugaz, N., Farrugia, C.J., Davies, J.A., Temmer, M., Veronig, A.M., et al., (2011), Arrival Time Calculation for Interplanetary Coronal Mass Ejections with Circular Fronts and Application to STEREO Observations of the 2009 February 13 Eruption. The Astrophysical Journal, 741, 34. DOI: https://doi.org/10.1088/0004-637X/741/1/34

Nieves-Chinchilla, T., R. Colaninno, A. Vourlidas, A. Szabo, R. P. Lepping, S. A. Boardsen, B. J. Anderson, and H. Korth (2012), Remote and in situ observations of an unusual Earth-directed coronal mass ejection frommultiple viewpoints, J. Geophys. Res., 117, A06106. DOI: https://doi.org/10.1029/2011JA017243

Paouris, E., Mavromichalaki, H. Interplanetary Coronal Mass Ejections Resulting from Earth-Directed CMEs Using SOHO and ACE Combined Data During Solar Cycle 23. Sol Phys 292, 30 (2017a). https://doi.org/10.1007/s11207-017-1050-2

Paouris, E., Mavromichalaki, H. Effective Acceleration Model for the Arrival Time of Interplanetary Shocks driven by Coronal Mass Ejections. Sol Phys 292, 180 (2017b). https://doi.org/10.1007/s11207-017-1212-2

Paouris, E., Čalogović, J., Dumbović, M. et al. Propagating Conditions and the Time of ICME Arrival: A Comparison of the Effective Acceleration Model with ENLIL and DBEM Models. Sol Phys 296, 12 (2021a). https://doi.org/10.1007/s11207-020-01747-4

Paouris, E., Vourlidas, A., Papaioannou, A., & Anastasiadis, A. (2021b). Assessing the projection correction of coronal mass ejection speeds on time-of-arrival prediction performance using the Effective Acceleration Model. Space Weather, 19, e2020SW002617. DOI: https://doi.org/10.1029/2020SW002617

Patsourakos, S., Vourlidas, A., Török, T., Kliem, B., Antiochos, S. K., Archontis, V., et al. (2020). Decoding the pre-eruptive magnetic field configurations of coronal mass ejections. Space Science Reviews. 216(8), 1–63. DOI: https://doi.org/10.1007/s11214-020-00757-9

Pulkkinen, A. A., Bisi, M. M., Luntama, J. P., Kraft, S., Glover, A., and Heil, M. (2019). "ESA Lagrange space weather monitoring mission to L5 point," in AGU Fall Meeting Abstracts (Washington, DC). Pulkkinen, A. A., Bisi, M. M., Luntama, J. P., Kraft, S., Glover, A., and Heil, M. (2019). "ESA Lagrange space weather monitoring mission to L5 point," in AGU Fall Meeting Abstracts (Washington, DC).

814 https://ui.adsabs.harvard.edu/abs/2019AGUFMSH24B..01Phttps://ui.adsabs.harvard.edu/abs/201
815 9AGUFMSH24B..01P

817 Reiner, M. J., Kaiser, M. L., & Bougeret, J.-L. (2007). Coronal and interplanetary propagation of
818 CME/shocks from radio, in situ and white-light observations. The Astrophysical Journal, 663,
819 1369–1385. DOI: https://doi.org/10.1086/518683

821 Richardson, I. G., Webb, D. F., Zhang, J., Berdichevsky, D. B., Biesecker, D. A., Kasper, J. C.,
822 Kataoka, R., Steinberg, J. T., Thompson, B. J., Wu, C. C., & Zhukov, A. N. (2006). Major
823 geomagnetic storms (Dst ≤ 100 nT) generated by corotating interaction regions. Journal of
824 Geophysical Research, 111, A07S09. https://doi.org/10.1029/2005JA011476

826 Riley, P., Mays, L., Andries, J., Amerstorfer, T., Biesecker, D., Delouille, V., et al. (2018). Fore-
827 casting the arrival time of coronal mass ejections: Analysis of the CCMC CME scoreboard.
828 Space Weather, 16, 1245–1260. DOI: https://doi.org/10.1029/2018SW001962

830 Rouillard, A. P., Davies, J. A., Forsyth, R. J., Rees, A., Davis, C. J., Harrison, R. A., ... & Perry,
831 C. H. (2008). First imaging of corotating interaction regions using the STEREO spacecraft.
832 Geophysical Research Letters, 35(10). DOI: https://doi.org/10.1029/2008GL033767

834 Sachdeva, N., Subramanian, P., Vourlidas, A., & Bothmer, V. (2017). CME dynamics using
835 STEREO and LASCO observations: the relative importance of Lorentz forces and solar wind
836 drag. Solar Physics, 292(9), 1-17. DOI: https://doi.org/10.1007/s11207-017-1137-9

838 Sheeley, N. R., Jr., J. H. Walters, Y.-M. Wang, and R. A. Howard (1999), Continuous tracking
839 of coronal outflows: Two kinds of coronal mass ejections, J. Geophys. Res., 104, 24,739–
840 24,767.

842 Sheeley, N.R. Jr., Herbst, A.D., Palatchi, C.A., Wang, Y.-M., Howard, R.A., et al.: 2008,
843 Heliospheric images of the solar wind at Earth. Astrophys. J. 675, 853. DOI:
844 https://doi.org/10.1086/526422

846 Temmer, M., Preiss, S., & Veronig, A. M. (2009). CME projection effects studied with
847 STEREO/COR and SOHO/LASCO. Solar Physics, 256, 183–199.
848 https://doi.org/10.1007/s11207-009-9336-7

850 Temmer, M., Reiss, M. A., Nikolic, L., Hofmeister, S. J., & Veronig, A. M. (2017).
851 Preconditioning of interplanetary space due to transient CME disturbances. The Astrophysical
852 Journal, 835(2), 141. DOI: https://doi.org/10.3847/1538-4357/835/2/141

854 Tsurutani, B. T., and W. D. Gonzalez (1997), The interplanetary causes of magnetic storms: A
855 review, in Magnetic Storms, Geophys. Monogr. Ser., vol. 98, edited by B. T. Tsurutani, W. D.
856 Gonzalez, Y. Kamide, and J. K. Arballo, p. 77, AGU, Washington, D. C.
857 Verbeke, C., Mays, M. L., Temmer, M., Bingham, S., Steenburgh, R., Dumbovic, M., et al.
858 (2019). Benchmarking CME arrival time and impact: Progress on metadata, metrics, and events.
859 Space Weather, 17. DOI: https://doi.org/10.1029/2018SW002046

Vourlidas, A., & Howard, R. A. (2006). The proper treatment of coronal mass ejection brightness: A new methodology and implications for observations. The Astrophysical Journal, 642(2), 1216. DOI: https://doi.org/10.1086/501122

Vourlidas, A., Lynch, B. J., Howard, R. A., & Li, Y. (2013). How many CMEs have flux ropes? Deciphering the signatures of shocks, flux ropes, and prominences in coronagraph observations of CMEs. Solar Physics, 284, 179–201. https://doi.org/10.1007/s11207-012-0084-8

Vourlidas, A., Balmaceda, L. A., Stenborg, G., and Dal Lago, A., Multi-viewpoint Coronal Mass Ejection Catalog Based on STEREO COR2 Observations, The Astrophysical Journal, vol. 838, no. 2, 2017. DOI: https://doi.org/10.3847/1538-4357/aa67f0.

Vourlidas, A., Patsourakos, S., & Savani, N. P. (2019). Predicting the geoeffective properties of coronal mass ejections: current status, open issues and path forward. Philosophical Transactions of the Royal Society A, 377(2148), 20180096. DOI: https://doi.org/10.1098/rsta.2018.0096

Vršnak, B., Ruždjak, D., Sudar, D., & Gopalswamy, N. (2004). Kinematics of coronal mass ejections between 2 and 30 solar radii-What can be learned about forces governing the eruption?, Astronomy & Astrophysics, 423(2), 717-728. DOI: https://doi.org/10.1051/0004-6361:20047169

Vršnak, B., Žic, T., Vrbanec, D., Temmer, M., Rollett, T., Möstl, C., ... & Shanmugaraju, A. (2013). Propagation of interplanetary coronal mass ejections: The drag-based model. Solar physics, 285(1), 295-315. DOI: https://doi.org/10.1007/s11207-012-0035-4

Winslow, R. M., N. Lugaz, L. C.Philpott, N. A. Schwadron, C. J.Farrugia, B. J. Anderson, andC. W. Smith (2015), Interplanetarycoronal mass ejections fromMESSENGER orbital observa-tions at Mercury, J. Geophys. Res.Space Physics, 120, 6101–6118. DOI: https://doi.org/10.1002/2015JA021200.

Wood, B.E., Wu, C.C., Lepping, R.P., Nieves-Chinchilla, T., Howard, R.A., Linton, M.G., Socker, D.G.: 2017, Astrophys. J. Suppl. 229, 29. DOI: https://iopscience.iop.org/article/10.3847/1538-4365/229/2/29

Zhang, J., Richardson, I.G.,Webb, D.F., Gopalswamy, N., Huttunen, E., Kasper, J.C., et al.: 2007, J. Geophys. Res. 112, A10102. DOI: https://doi.org/10.1029/2007JA012321